RSC Advances

PAPER

View Article Online
View Journal | View Issue

Cite this: *RSC Adv.*, 2022, **12**, 30764

Theoretical study on the stability, ferroelectricity and photocatalytic properties of $CaBiO_3$

Xiang-Fu Xu,[a] Li-Fang Chen,[a] Hua-Kai Xu,[a] Guo-Xia Lai,[a] Su-Mei Hu,[a] Hong Ji,[a] Jia-Jun Tang,[b] Xing-Yuan Chen *[a] and Wei-Ling Zhu*[a]

Received 8th September 2022
Accepted 17th October 2022

DOI: 10.1039/d2ra05660g

rsc.li/rsc-advances

Materials with high ferroelectric polarization strength and sufficient absorption of visible light have unique advantages in photocatalysis. Based on the results of structure search, phonon frequency, and elasticity coefficient calculations, $CaBiO_3$ has a stable *R*3 polar structure. First-principles calculations indicate that *R*3-$CaBiO_3$ is a potentially efficient ferroelectric visible-light photocatalytic material for hydrogen production. $CaBiO_3$ under slight strain can maintain high ferroelectric polarization strength, strong visible light absorption capacity and small effective mass. $CaBiO_3$ under tensile strain has potentially ferroelectric photogeneration of hydrogen with a band edge position that crosses the redox potential of water. These results can expand the application of Bi-based materials in photocatalytic hydrogen production.

1. Introductions

Perovskite oxides exhibit a wide range of ferroelectric, piezoelectric, and thermoelectric characteristics as well as electro-optical effects, which makes them a focus in the photovoltaic and photocatalysis fields.[1–3] Ferroelectric materials display spontaneous polarization due to the offset of positive and negative charge centers, providing a new prospect for photovoltaic device design by promoting the separation of photoexcited carriers.[4] In addition, the internal electric field of ferroelectric polarization also enhances inhibition of the recombination of electrons and holes.[5] Ferroelectric materials can also serve as new candidates for photocatalysis, similar to the P–N junction mechanisms, which significantly impact surface photochemistry.[6] The non-polluting hydrogen energy generated by photocatalysis is one of the mainstays of future energy development.[7] The spontaneous polarization of ferroelectrics can provide a strong internal electric field for the photocatalytic water separation process, which are beneficial for photocatalytic hydrogen production.[8] Bismuth-based semiconductors have attracted extensive attention for their excellent photocatalytic performance under visible light due to Bi ions' unique 6s and 6p orbitals.[9,10] First-principle calculation results show that $CaBiO_3$ has a potentially stable *R*3 ferroelectric structure,[11,12] an excellent visible light-absorbing material with a bandgap of about 1.8 eV.[11] Rokesh *et al.* synthesized $CaBiO_3$ through glycine-complexation (GC) and ion-exchange (IE) methods and found that it can generate highly reactive photocatalytic free radicals to degrade pollutants.[13] For semiconductor materials to meet the conditions of photocatalytic hydrogen production, the bandgap must be larger than the standard Gibbs free energy change for the decomposition of water into H_2 and O_2, while the band edge position must extend across the redox potential of water.[14] The $CaBiO_3$ crystal structure search is processed using the evolutionary algorithm implemented in the USPEX code[15–17] in this paper. The stability of $CaBiO_3$ is further verified by phonon frequencies and elasticity coefficients. Our calculation results show that $CaBiO_3$ under tensile conditions has excellent potential as a new ferroelectric photocatalytic semiconductor material for hydrogen production.

2. Calculation method

The stable structure of $CaBiO_3$ is searched by USPEX code with 20 atoms. The initial structure of the first generation is set as 300, and that of the second generation is 50. The convergence standard remains unchanged for the 10th generation. Variables of 50% genetic, 20% random, 20% soft mode mutation, and 10% lattice mutation were set in the calculation. As shown in Table 1, the stable structure space group number of $CaBiO_3$ is 146 (*R*3 space group), which consistent with earlier theories and experimental reports.[11–13] The calculated $CaBiO_3$ structure by USPEX software is transformed into a conventional cell structure as shown in Fig. 1. The calculated lattice parameters a and *c* of $CaBiO_3$ are 5.88 Å and 15.47 Å respectively, which is closed to the early reports in the literature (a = 5.81 Å, c = 15.22 Å).[11] The electronic structure, elastic properties, and photoelectric properties of *R*3 space group $CaBiO_3$ are calculated using first-principles software packaged in VASP.[18] The PAW pseudopotential method is used to describe the interaction between electrons and nuclei,[19] and the exchange-correlation functional between electrons is

[a]*Department of Physics, School of Science, Guangdong University of Petrochemical Technology, Maoming, Guangdong 525000, PR China. E-mail: chenxingyuan@gdupt.edu.cn; zhuweiling@gdupt.edu.cn; Fax: +86-668-2923567; Tel: +86-668-2923838*

[b]*Department of Physics, South China University of Technology, Guangzhou 510640, PR China*

Table 1 The structure search for $CaBiO_3$ by USPEX code

Gen	ID	Origin	Enthalpy (eV)	Volume (A^3)	Density (g cm^{-3})	SYMM
1	7	Random	−119.029	305.066	6.468	5
2	55	Heredity	−119.863	309.169	6.382	146
3	120	keptBest	−119.863	309.169	6.382	146
4	166	keptBest	−119.863	309.169	6.382	146
5	212	keptBest	−119.863	309.169	6.382	146
6	258	keptBest	−119.863	309.169	6.382	146
7	304	keptBest	−119.863	309.169	6.382	146
8	351	keptBest	−119.863	309.169	6.382	146
9	397	keptBest	−119.863	309.169	6.382	146
10	444	keptBest	−119.863	309.169	6.382	146
11	494	keptBest	−119.863	309.169	6.382	146

treated by Perdew–Burke–Ernzerhof (PBE) functional.[20] The cutoff energy was taken at 520 eV, and the Monkhorst–Pack *k*-point sampling was given as 0.03 $Å^{-1}$ in the calculation. The energy and force convergence criteria are set as 10^{-6} eV and 10^{-2} eV $Å^{-1}$, respectively. The bandgap and absorption spectra of $CaBiO_3$ are calculated by Modified Becke–Johnson (MBJ) exchange potential since PBE functional usually underestimates the bandgap of the material.[21] Parameter C in the MBJ functional was set as 1.7, and the bandgap result calculated was close to the earlier hybrid HSE functional (Heyd–Scuseria–Ernzerhof) report result.[11] The strain is introduced by changing the lattice parameters of *a* and *b* to relax the *c* axis in Fig. 1. Lattice parameters *a* and *b* are increased by 2% to relax the *c* lattice parameter, indicating the introduction of 2% tensile strain. The calculated lattice parameters *a* and *c* of $CaBiO_3$ under 2% tensile strain become 6.00 Å and 15.14 Å respectively. Lattice parameters *a* and *b* are reduced by 2% to relax lattice parameter *c*, representing the introduction of 2% compressive strain. The calculated lattice parameters *a* and *c* of $CaBiO_3$ under 2% compressive strain become 5.76 Å and 15.87 Å respectively. T-$CaBiO_3$ represents the introduction of tensile strain in $CaBiO_3$, while C-$CaBiO_3$ represents the introduction of compressive strain in $CaBiO_3$.

3. Stability analysis

The search results for USPEX suggest that $CaBiO_3$ with *R*3 space group is a potentially stable structure. The elastic properties and phonon frequencies of $CaBiO_3$ with *R*3 space group are calculated to verify the stability furtherly. $CaBiO_3$ with *R*3 space group has seven independent elastic coefficients. The

Table 2 The calculated elastic coefficient (GPa)

	C_{11}	C_{12}	C_{13}	C_{14}	C_{15}	C_{33}	C_{44}	C_{66}
$CaBiO_3$	180.4	86.4	69.0	0.9	6.3	121.8	48.4	47.0
C-$CaBiO_3$	181.6	96.6	78.3	3.7	6.9	136.4	52.4	42.5
T-$CaBiO_3$	175.2	77.6	63.6	0.2	6.4	113.2	44.3	48.8

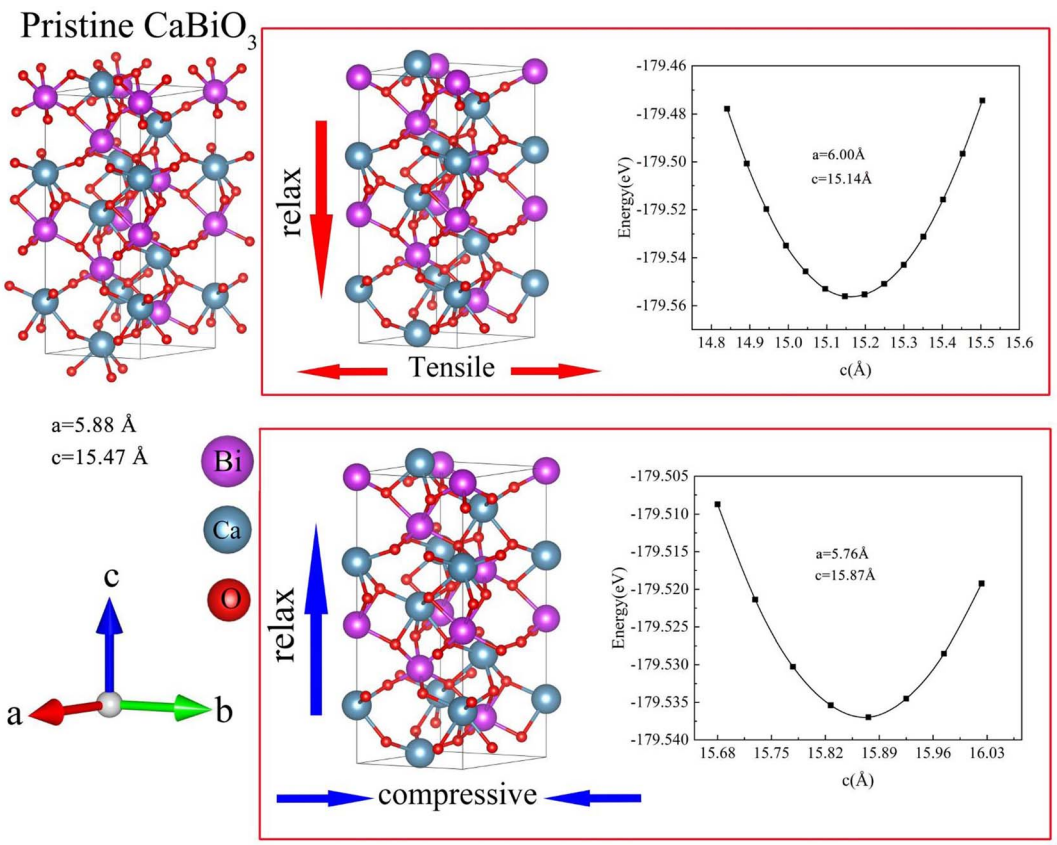

Fig. 1 The structure and lattice parameters of pristine *R*3-$CaBiO_3$ and *R*3-$CaBiO_3$ under strain.

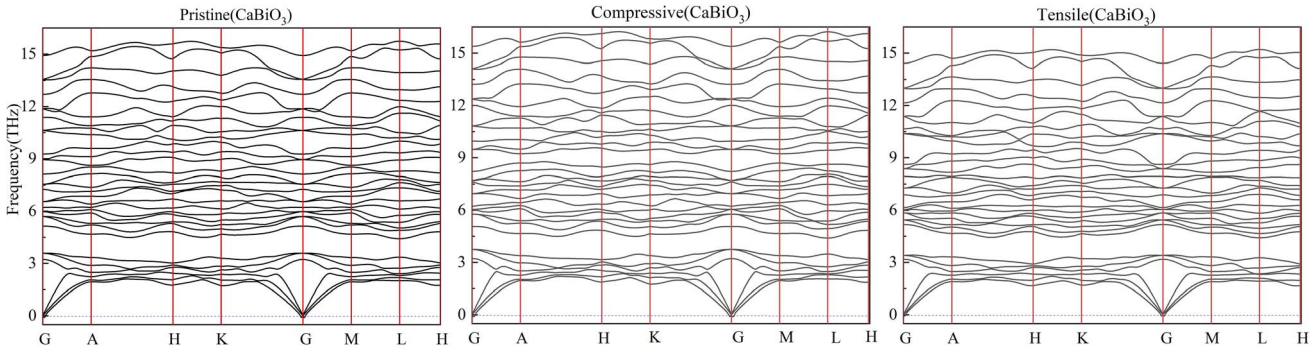

Fig. 2 The calculated phonon frequencies.

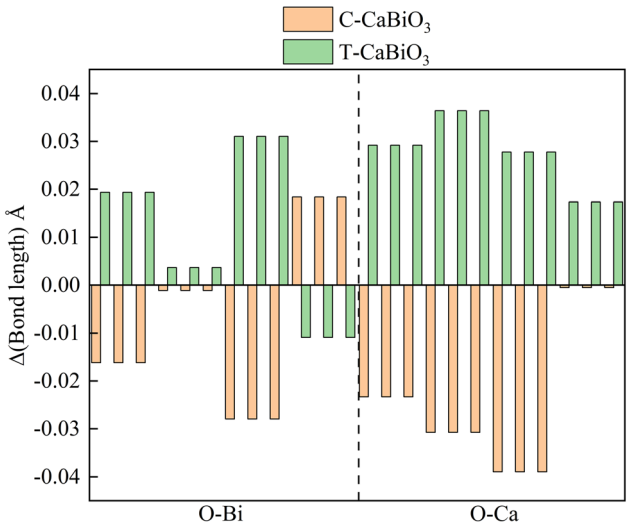

Fig. 3 The bond length differences (Δ) of Bi-O (left) and Ca-O (right) relative to pristine $CaBiO_3$ under strain.

independent elastic coefficients must satisfy the following inequalities group (1) to achieve mechanical stability.[22]

$$\begin{aligned} &C_{11} > |C_{12}| \\ &C_{13}2 < 0.5 \times C_{33}(C_{11} \times C_{12}) \\ &C_{14}2 + C_{15}2 < 0.5 \times C_{44} \times (C_{11} - C_{12}) \\ &C_{44} > 0 \end{aligned} \quad (1)$$

The calculated elastic coefficients are shown in Table 2, which meet all the requirements of the inequality group for mechanical stability. 2 × 2 × 2 supercell contained 80 atoms have been used to calculate the phonon frequency of pristine $CaBiO_3$ and $CaBiO_3$ under strain conditions. The calculated phonon frequency of pristine $CaBiO_3$ with the *R*3 space group in Fig. 2 shows that there is no imaginary frequency in the whole Brillouin region, indicating that it is a potentially metastable structure. $CaBiO_3$ under compressive or tensile strain conditions can still maintain stability due to the calculated elastic coefficients and phonon frequency results in Table 2 and Fig. 2. The elastic coefficients and phonon frequency of $CaBiO_3$ under compressive strain condition become larger since the shorter bond lengths of Ca–O and Bi–O in the Fig. 3 could lead to the increased atomic interactions. Conversely, the tensile strain effect causes the bond length of $CaBiO_3$ to be larger for reducing the atomic interactions, which leading to the lower elastic coefficients and phonon frequencies.

Table 3 The calculated displacement offset between the polar structure and centrosymmetric structure

	Ca (Å)	Bi (Å)	O (Å)
$CaBiO_3$	−0.4	0.13	0.43
C-$CaBiO_3$	−0.46	0.13	0.44
T-$CaBiO_3$	−0.34	0.13	0.42

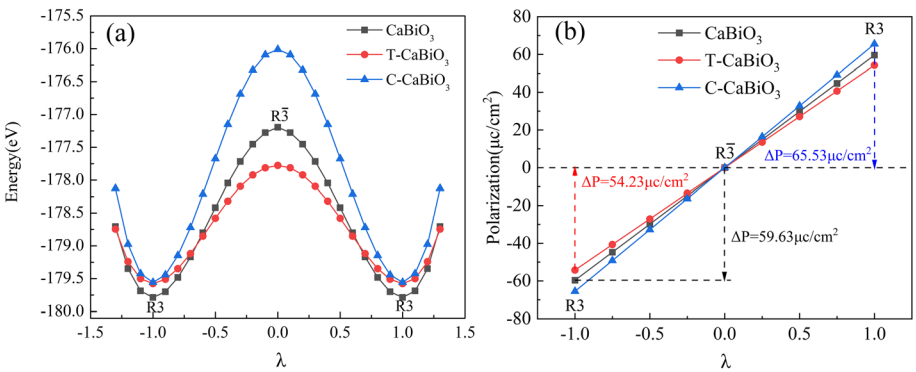

Fig. 4 The (a) calculated energy and (b) ferroelectric polarization strength with the movement of atoms. λ is the atom displacement interpolation between ferroelectric (1) and paraelectric states (0) states.

4. Calculated ferroelectric properties

The ferroelectric properties of the $R3$-$CaBiO_3$ polarized structure are calculated by the modern polarization theory of the Berry Phase method,[23,24] and $R\bar{3}$ is chosen as the centrosymmetric phase. The calculation results are shown in Fig. 4, and λ is the linear interpolation scale value between the polarized and centrosymmetric phase structures. $R3$-$CaBiO_3$ forms a noticeable

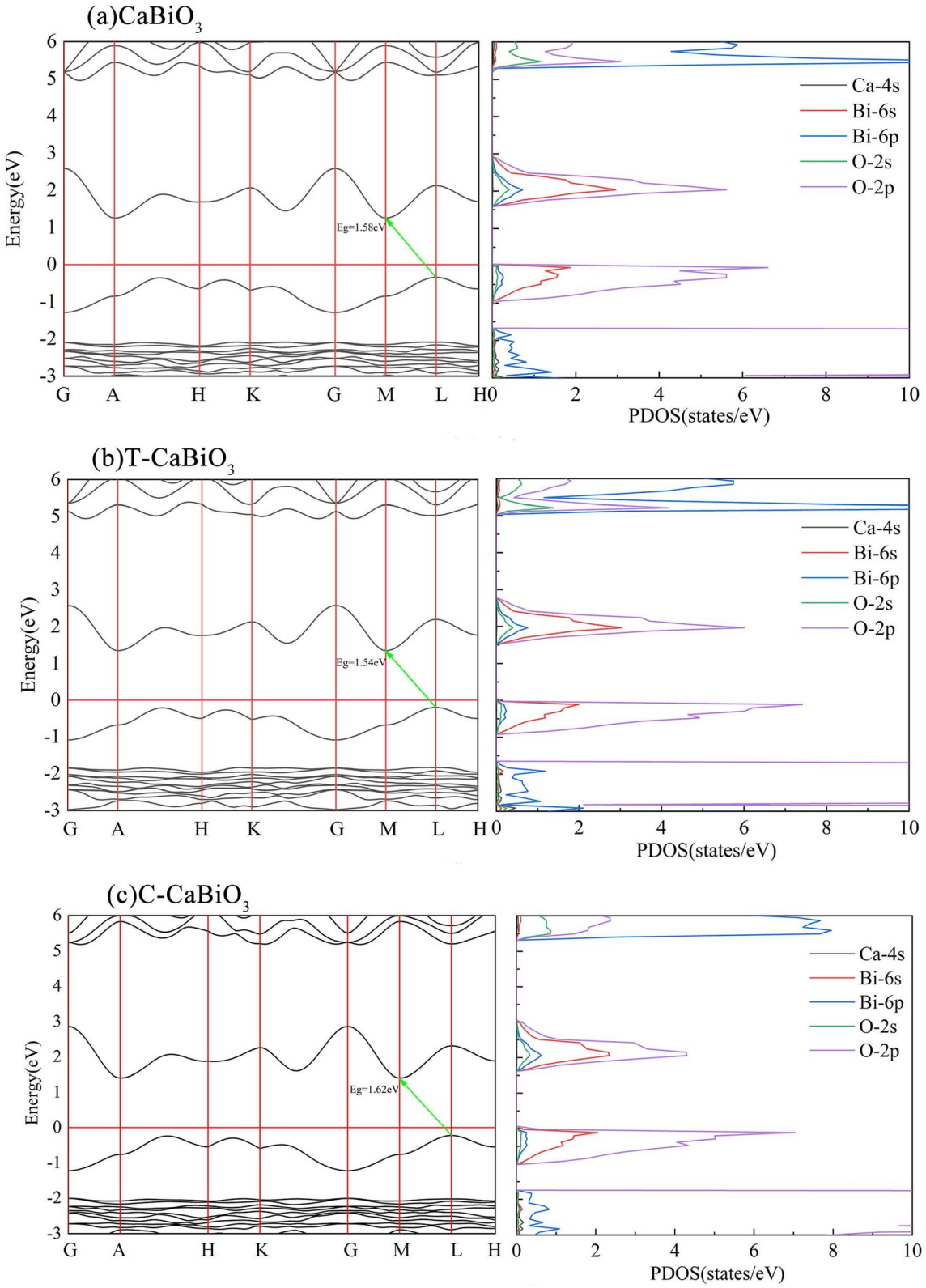

Fig. 5 The calculated energy band structure and density of states.

double potential well curve with atomic movement, and the position of the potential well represents the ferroelectric polarized phase. The calculated ferroelectric polarization strength is 59.63 μc cm^{-2}, which is close to the value of 56 μc cm^{-2} reported in the earlier literature,[11] and close to the ferroelectric polarization strength of conventional ferroelectric oxide *R*3*c* $ZnSnO_3$.[25,26] Next, we consider the effect of strain on the ferroelectric properties of *R*3-$CaBiO_3$. *R*3-$CaBiO_3$, under the presence of a slight strain, can still maintain ferroelectric polarization strength larger than 50 μc cm^{-2} as well. The ferroelectric driving mechanism of *R*3-$CaBiO_3$ is similar to that of the *R*3*c* structures $BiFeO_3$ and $ZnSnO_3$, which is mainly determined by the action of the A-site ions (Ca, Bi or Zn) and O ions.[27,28] The offset of Ca ions decreases from 0.40 Å to 0.34 Å under 2% tensile strain in Table 3, which reduces the ferroelectric polarization strength. The offset of Ca ions increases to 0.46 Å under compressive strain, which improves the ferroelectric polarization strength. Ca ion at A site of $CaBiO_3$ under strain conditions has the most direct effect on the ferroelectric properties of the system.

5. Discussions on photocatalytic properties

The optical properties of materials are closely related to the band structure. As shown in Fig. 5, the calculated energy band structure of $CaBiO_3$ is an indirect bandgap. Although an indirect bandgap is not an optimal function for light absorption, it could reduce the probability of photoelectron-hole radiation recombination. The calculated band gap of the pristine $CaBiO_3$ is 1.58 eV by MBJ functional, which is consistent with the value reported by HSE functional in the literature.[11] The optical absorption properties of the material are closely related to the bandgap of the material itself. In order to further understand the absorption of visible light, we also calculated the optical absorption spectrum. The relation between the optical absorption coefficient $\alpha(\omega)$ of $CaBiO_3$ and the real ε_r and the imaginary ε_i of the dielectric function is shown below eqn (2).

$$\alpha(\omega) = \frac{2\omega}{c}\left(\frac{\sqrt{\varepsilon_r^2(\omega)+\varepsilon_i^2(\omega)}-\varepsilon_r^2(\omega)}{2}\right)^{\frac{1}{2}} \quad (2)$$

ω is the circular photon frequency, and C is the speed of light. The pristine $CaBiO_3$ begins to absorb visible light when the incident photon energy is close to 1.6 eV and forms the prominent absorption peak (about 2.2 eV) in Fig. 6, indicating that it has a strong visible light absorption capacity. The slight red shift appears in the absorption coefficient of $CaBiO_3$ under tensile strain due to the longer bong length and lower band gap, while the opposite reaction occurs in the compressive strain condition.

The band edge of $CaBiO_3$ was calculated according to the following empirical formula[29] to explore the photocatalytic hydrogen production ability of $CaBiO_3$.

$$E_{CBM} = \chi + 0.5E_g + E_0 \quad (3)$$

$$E_{VBM} = \chi - 0.5E_g + E_0 \quad (4)$$

where E_g is the bandgap, χ is the mean electronegativity, and E_0 is the frame of reference as a scale factor concerning the normal hydrogen electrode (NHE) of the vacuum. As shown in Fig. 7, the CBM band edge position of pristine $CaBiO_3$ is close to the reduction potential of H^+/H_2, while the band edge position of VBM is lower than the oxidation potential of O_2/H_2O, showing a potential photocatalytic hydrogen production capacity. The empirical formula above was also used for the band edge positions of photocatalytic materials TiO_2, $NaBiO_3$, and $KBiO_3$.[30–32] Their band edge positions all cross the redox potential of water and satisfy the condition of decomposition water to produce hydrogen. The calculated density of the state of $CaBiO_3$ shows that the conduction band and valence band are mainly composed of O-2p and Bi-6s orbitals, which is similar to other Bi-based photocatalytic materials.[33] The effective mass of the electron in $CaBiO_3$ under strain conditions is also relatively small, which is close to $NaBiO_3$ (0.4 m_0) and $KBiO_3$ (0.8 m_0), as shown in Table 4, suggesting that the photogenerated carriers

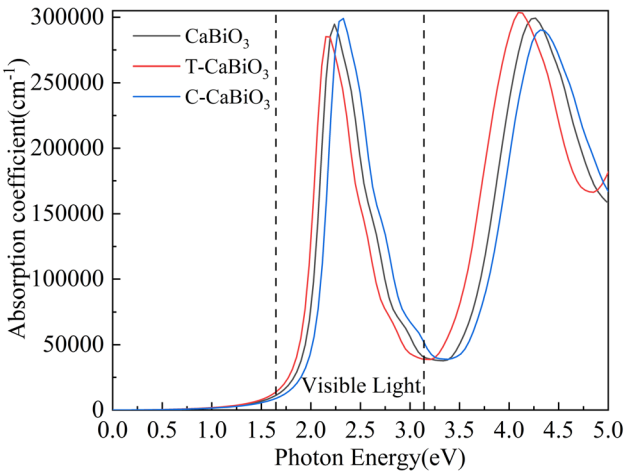

Fig. 6 The calculated optical absorption coefficient. The range of visible light is indicated between the two dashed lines.

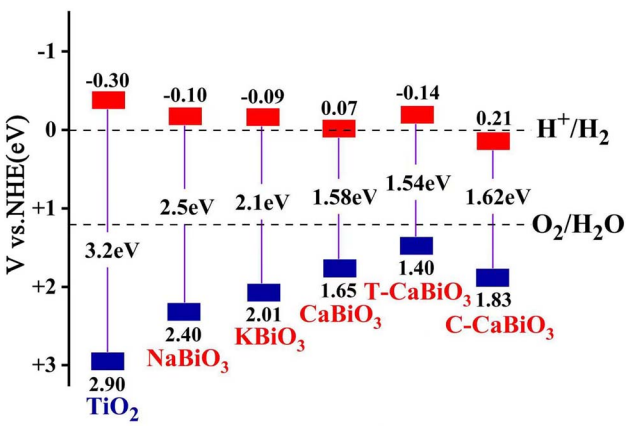

Fig. 7 The calculated band edge position for water oxidation–reduction potential.

Table 4 The calculated effective mass and the ratio of the hole effective mass to the electron effective mass (D)

	$CaBiO_3$	T-$CaBiO_3$	C-$CaBiO_3$	$NaBiO_3$	$KBiO_3$	$BaTiO_3$
Electron (m_0)	0.49	0.51	0.48	0.4 (ref. 33)	0.8 (ref. 33)	1.11 (ref. 34)
Hole (m_0)	1.34	1.47	1.23			2.69
D	2.73	2.88	2.56			2.44

of $CaBiO_3$ could be easy to separate. The higher transfer rate of photogenerated carriers and lower recombination rate could be produced due to the larger D value. D is defined as the ratio of the hole effective mass to the electron effective mass. The D values of $CaBiO_3$ at a slight strain in Table 4 range from 2.5 to 2.8, which is slightly larger than that of the conventional photocatalytic ferroelectric material $BaTiO_3$ ($D = 2.44$) calculated by the MBJ functional.[34,35] Meanwhile, the large ferroelectric strength and strong visible light absorption of $CaBiO_3$ will further contribute to the improvement of photocatalytic performance. The band edge positions of T-$CaBiO_3$ and C-$CaBiO_3$ are corrected by the 1 s core energy level of Bi atoms in pristine $CaBiO_3$. As shown in Fig. 7, the CBM band edge position of $CaBiO_3$ under the tensile strain condition moves up and becomes higher than the hydrogen reduction potential, which could be favorable to hydrogen production. The CBM band edge of C-$CaBiO_3$ moved down and was lower than hydrogen reduction potential, which reduced hydrogen production efficiency. $CaBiO_3$ under tensile strain can still maintain high ferroelectric polarization strength and strong visible light absorption ability, further promoting photocatalytic hydrogen production.

6. Conclusion

The USPEX software was used to explore the $CaBiO_3$ structure in this paper. The results show that the stable structure of $CaBiO_3$ is the $R3$ space group configuration. The phonon frequencies and elasticity coefficients calculations also indicate that $R3$-$CaBiO_3$ satisfies the stability condition. The ferroelectric polarization of $R3$-$CaBiO_3$ is mainly generated by the shift of the symmetry center of Ca-O ions. The shift of Ca ions significantly affects the ferroelectric polarization of $R3$-$CaBiO_3$ under strain conditions. The offset of Ca ions decreases under tensile strain with reduced ferroelectric polarization strength, while the opposite case is in the compressive strain condition. $R3$-$CaBiO_3$ can preserve the high ferroelectric polarization strength and visible light absorption capacity under the slight strain. The band edge position of $CaBiO_3$ under tensile strain can cross the redox potential of water and maintain a small electron-effective mass with the large ratio of hole and electron masses, which is favorable for photocatalytic hydrogen production. $CaBiO_3$ is a potential ferroelectric photocatalytic material for hydrogen production under visible light.

Conflicts of interest

The authors declared that they have no conflicts of interest to this work. We declare that we do not have any commercial or associative interest that represents a conflict of interest in connection with the work submitted.

Acknowledgements

This work was supported by Guangdong Province Natural Science Foundation of China (No. 2019A1515010914 and 2019A1515010916), Guangdong Province Special Foundation of Scientific and Technological Innovation (Grant No. 2021S055).

References

1 I. Grinberg, D. V. West, M. Torres, *et al.*, Perovskite oxides for visible-light-absorbing ferroelectric and photovoltaic materials, *Nature*, 2013, **503**(7477), 509–512.
2 B. Weng, Z. Xiao, W. Meng, *et al.*, Bandgap engineering of barium bismuth niobate double perovskite for photoelectrochemical water oxidation, *Adv. Energy Mater.*, 2017, **7**(9), 1602260.
3 W. J. Yin, B. Weng, J. Ge, *et al.*, Oxide perovskites, double perovskites and derivatives for electrocatalysis, photocatalysis, and photovoltaics, *Energy Environ. Sci.*, 2019, **12**(2), 442–462.
4 Y. Yuan, Z. Xiao, B. Yang, *et al.*, Arising applications of ferroelectric materials in photovoltaic devices, *J. Mater. Chem. A*, 2014, **2**(17), 6027–6041.
5 L. Li, P. A. Salvador and G. S. Rohrer, Photocatalysts with internal electric fields, *Nanoscale*, 2014, **6**(1), 24–42.
6 H. K. Christenson and N. H. Thomson, The nature of the air-cleaved mica surface, *Surf. Sci. Rep.*, 2016, **71**(2), 367–390.
7 J. Zhang, W. Hu, S. Cao, *et al.*, Recent progress for hydrogen production by photocatalytic natural or simulated seawater splitting, *Nano Res.*, 2020, **13**(9), 2313–2322.
8 Y. Li, J. Li, W. Yang, *et al.*, Implementation of ferroelectric materials in photocatalytic and photoelectrochemical water splitting, *Nanoscale Horiz.*, 2020, **5**(8), 1174–1187.
9 X. Meng and Z. Zhang, Bismuth-based photocatalytic semiconductors: introduction, challenges and possible approaches, *J. Mol. Catal. A: Chem.*, 2016, **423**, 533–549.
10 D. Cui, L. Wang, Y. Du, *et al.*, Photocatalytic reduction on bismuth-based p-block semiconductors, *ACS Sustainable Chem. Eng.*, 2018, **6**(12), 15936–15953.
11 J. He, C. Franchini and J. M. Rondinelli, Ferroelectric oxides with strong visible-light absorption from charge ordering, *Chem. Mater.*, 2017, **29**(6), 2445–2451.
12 A. Smolyanyuk, C. Franchini and L. Boeri, Ab initio study of A BiO_3 (A= Ba, Sr, Ca) under high pressure, *Phys. Rev. B: Condens. Matter Mater. Phys.*, 2018, **98**(11), 115158.

13 K. Rokesh, M. Sakar and T. O. Do, Calcium Bismuthate ($CaBiO_3$): A Potential Sunlight-Driven Perovskite Photocatalyst for the Degradation of Emerging Pharmaceutical Contaminants, *ChemPhotoChem*, 2020, **4**(5), 373–380.

14 F. E. Osterloh, Inorganic nanostructures for photoelectrochemical and photocatalytic water splitting, *Chem. Soc. Rev.*, 2013, **42**(6), 2294–2320.

15 A. R. Oganov, A. O. Lyakhov and M. Valle, How evolutionary crystal structure prediction works—and why, *Acc. Chem. Res.*, 2011, **44**, 227–237.

16 A. R. Oganov and C. W. Glass, Crystal structure prediction using ab initio evolutionary techniques: principles and applications, *J. Chem. Phys.*, 2006, **124**, 244704.

17 A. O. Lyakhov, A. R. Oganov, H. T. Stokes, *et al.*, New developments in evolutionary structure prediction algorithm USPEX, *Comput. Phys. Commun.*, 2013, **184**(4), 1172–1182.

18 G. Kresse and J. Furthmüller, Efficient iterative schemes for ab initio total-energy calculations using a plane-wave basis set, *Phys. Rev. B: Condens. Matter Mater. Phys.*, 1996, **54**, 11169.

19 P. E. Blöchl, Projector augmented-wave method, *Phys. Rev. B: Condens. Matter Mater. Phys.*, 1994, **50**, 17953.

20 J. P. Perdew, K. Burke and M. Ernzerhof, *Phys. Rev. Lett.*, 1996, **77**, 3865–3868.

21 F. Tran and P. Blaha, Accurate band gaps of semiconductors and insulators with a semilocal exchange-correlation potential, *Phys. Rev. Lett.*, 2009, **102**(22), 226401.

22 F. Mouhat and F. X. Coudert, Necessary and sufficient elastic stability conditions in various crystal systems, *Phys. Rev. B: Condens. Matter Mater. Phys.*, 2014, **90**(22), 224104.

23 R. D. King-Smith and D. Vanderbilt, Theory of polarization of crystalline solids, *Phys. Rev. B: Condens. Matter Mater. Phys.*, 1993, **47**(3), 1651.

24 R. Resta, Macroscopic polarization in crystalline dielectrics: the geometric phase approach, *Rev. Mod. Phys.*, 1994, **66**(3), 899.

25 J. Y. Son, G. Lee, M. H. Jo, *et al.*, Heteroepitaxial ferroelectric $ZnSnO_3$ thin film, *J. Am. Chem. Soc.*, 2009, **131**(24), 8386–8387.

26 M. Nakayama, M. Nogami, M. Yoshida, *et al.*, First-Principles Studies on Novel Polar Oxide $ZnSnO_3$; Pressure-Induced Phase Transition and Electric Properties, *Adv. Mater.*, 2010, **22**(23), 2579–2582.

27 P. Baettig, C. Ederer and N. A. Spaldin, First-principles study of the multiferroics $BiFeO_3$, Bi_2Fe CrO_6, and $BiCrO_3$: Structure, polarization, and magnetic ordering temperature, *Phys. Rev. B: Condens. Matter Mater. Phys.*, 2005, **72**(21), 214105.

28 J. Zhang, K. L. Yao, Z. L. Liu, *et al.*, First-principles study of the ferroelectric and nonlinear optical properties of the $LiNbO_3$-type $ZnSnO_3$, *Phys. Chem. Chem. Phys.*, 2010, **12**(32), 9197–9204.

29 Y. Xu and M. A. A. Schoonen, The absolute energy positions of conduction and valence bands of selected semiconducting minerals, *Am. Mineral.*, 2000, **85**(3-4), 543–556.

30 J. Zhang, P. Zhou, J. Liu, *et al.*, New understanding of the difference of photocatalytic activity among anatase, rutile and brookite TiO_2, *Phys. Chem. Chem. Phys.*, 2014, **16**(38), 20382–20386.

31 H. Zheng, T. Zhang, Y. Zhu, *et al.*, $KBiO_3$ as an Effective Visible-Light-Driven Photocatalyst: Degradation Mechanism for Different Organic Pollutants, *ChemPhotoChem*, 2018, **2**(5), 442–449.

32 J. Liu, S. Chen, Q. Liu, *et al.*, Correlation of crystal structures and electronic structures with visible light photocatalytic properties of $NaBiO_3$, *Chem. Phys. Lett.*, 2013, **572**, 101–105.

33 Z. Xu, K. Xu, H. Feng, *et al.*, Sp orbital hybridization: a strategy for developing efficient photocatalysts with high carrier mobility, *Sci. Bull.*, 2018, **63**, 465–468.

34 W. Zulfiqar, S. M. Alay-e-Abbas, G. Abbas, *et al.*, Revisiting the structural, electronic and photocatalytic properties of Ti and Zr based perovskites with meta-GGA functionals of DFT, *J. Mater. Chem. C*, 2021, **9**(14), 4862–4876.

35 W. Zulfiqar and S. M. Alay-e-Abbas, Improved thermodynamic stability and visible light absorption in Zr + X codoped (X = S, Se and Te) $BaTiO_3$ photocatalysts: a first-principles study, *Mater. Today Commun.*, 2022, **32**, 103867.